Supplemental Material

Marangoni-Induced Reversal of Meniscus-Climbing Microdroplets

Jianxing Sun[1], Patricia B. Weisensee[1,2,*]

[1]*Department of Mechanical Engineering & Materials Science, Washington University in St. Louis, St. Louis, Missouri 63130, USA*

[2]*Institute of Materials Science and Engineering, Washington University in St. Louis, St. Louis, Missouri 63130, USA*

* Corresponding author: p.weisensee@wustl.edu

Content

S1. Characterization of Glaco and oil coatings

S2. Capillary-suction-induced oil meniscus flow velocity

S3. Conversion of radial velocity U_r into interfacial velocity U_M

S4. Simulation of heat transfer and fluid dynamics within an oil meniscus

S5. Influence of thermal conductivity of the central sphere on oil convection

S6. Negative convection rolls in an oil meniscus on a heated substrate

S7. Estimation of ($\cos \varphi_F - \cos \varphi_B$) for small floating droplets

S8. Dynamics of droplets initially dispensed closer to the meniscus top

S9. Determination of fitting factor f

Video 1 Comparison of microdroplet movements on an oil meniscus (Krytox GPL 102, 53 cP) surrounding a 780-µm borosilicate glass sphere on room temperature and cooled (8 °C) sapphire substrates, respectively.

Video 2 Marangoni convection in a silicone oil (19 cP) meniscus surrounding a non-volatile ethylene-glycol droplet ($D \approx 700$ µm) on heated (50 °C) and cooled (5 °C) sapphire substrates (both at steady state).

Video 3 Marangoni convection in an oil meniscus surrounding a water droplet sitting on a glass bottom petri dish pre-wetted with 19 cP silicone oil at room temperature. The dish cover is initially closed and then opened, which changes the water droplet's evaporation rate and latent cooling.

Video 4 Bidirectional movements of condensed microdroplets during water condensation on a cooled sapphire substrate infused with 9.3 cP silicone oil. The temperatures of substrate and water vapor (using nitrogen as carrier gas) are set at 10 °C and 40 °C, respectively.

S1. Characterization of Glaco and oil coatings

The scanning electron microscope (SEM) images of **Fig. S1(a)** show a layer of the uniform porous Glaco coating in cross-sectional and top views. The contact angle for a millimetric water droplet on the Glaco-coated surface is $165 \pm 3°$. We applied thin layers of oil ($5 - 27$ μm) on the textured surfaces *via* spin coating at 600-1000 rpm. To coat thicker oil films ($28 - 50$ μm), we applied a known amount of oil to the sample and let the oil even out overnight (oil has a positive spreading coefficient on Glaco and hence fully wets the sample). We weighed the mass of the oil using an analytical balance (OHAUS Pioneer PA64) and calculated the oil film thickness based on the substrate dimensions. **Figure S1(b)** shows the correlation between spin speed, oil mass, and oil film thickness. The accuracy of the correlation and the repeatability of the oil thickness using both approaches were confirmed using a confocal fluorescence microscope (LSM 880 Airyscan, Carl Zeiss), where silicone oils were dyed with Lumogen Rot F305. Based on the similarity in viscosity and surface tension, we assume that the thickness of the Krytox oil is approximately the same.
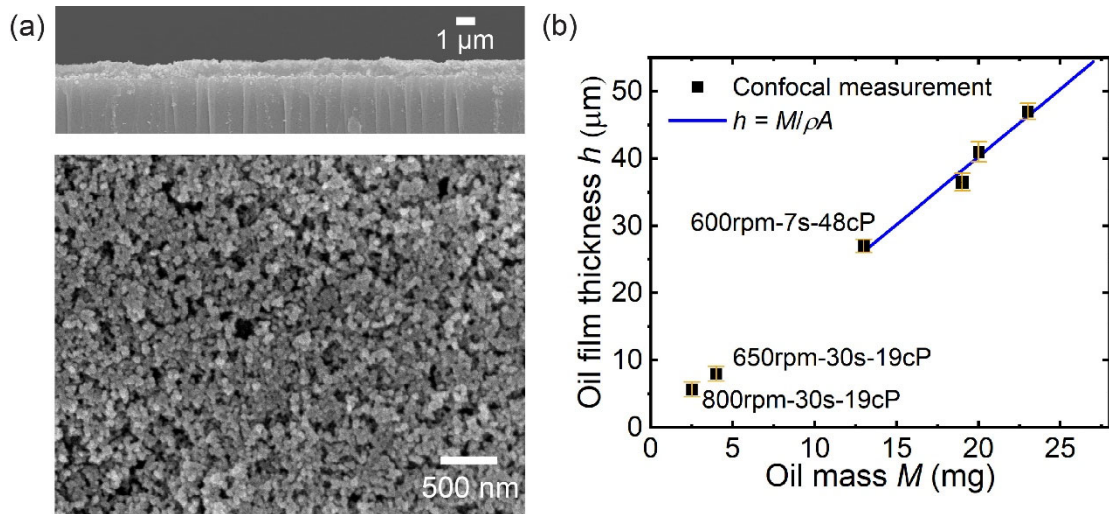

Figure S1. Characterization of the superhydrophobic coating and oil film thickness. (a) Scanning electron microscope (SEM) images of the Glaco coating in cross-sectional (top) and top (bottom) views. (b) Oil film thickness vs. mass of oil. The oil film thickness was measured using confocal microscopy to validate the accuracy and repeatability of the coating methods.

S2 Capillary-suction-induced oil meniscus flow velocity

The dynamic growth and final size of the oil meniscus significantly depends on the amount of lubricant available in the system[1,2]. In our experiments, the initial oil film thickness of the samples is thick and central objects are sub-millimetric, featuring an oversaturated system. The growth speed of the meniscus is thus relatively fast. As shown in **Fig. S2**, the pressure-driven flow velocity quickly decreases to 2 μm/s at $t = 20$ mins, where $t = 0$ min represents the moment when the glass sphere is placed on the substrate.
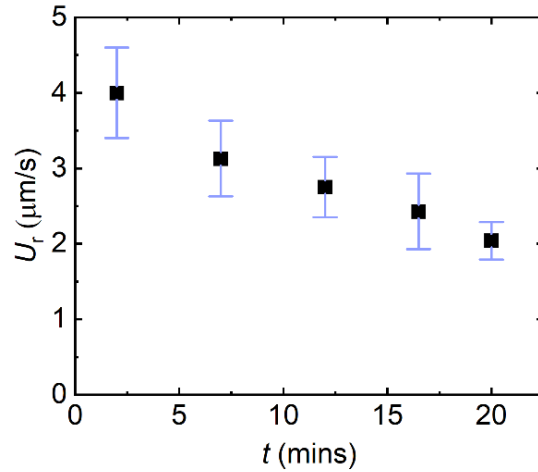
Figure S2. Capillary-suction-induced oil meniscus flow velocity changes over time. The velocity was measured via confocal microscopy, where the silicone oil (19 cP) was dyed with Lumogen Rot F305 and labeled with a low concentration of 1-µm Fluoresbrite YG microspheres. The initial oil film thickness was about 41 µm. The central object was a 750-um glass sphere and the substrate was kept at room temperature. At minimum of five locations were measured for each time point and the error bar represents the velocity range.

S3 Conversion of radial velocity U_r into interfacial velocity U_M

We experimentally measured the radial velocity U_r of particles inside oil menisci and found that the maximum values of U_r primarily occurred in the green shade region marked in **Fig. S3(a)**. The interfacial velocity $U_M = U_r / \cos\alpha$, where α denotes the meniscus slope angle. Based on geometrical considerations, we can approximate $\beta \approx \psi = \arctan(2h_m/L)$. **Figure S3(b)** shows a meniscus profile in side-view and the location of maximum U_r, substantiating the geometry relationship.
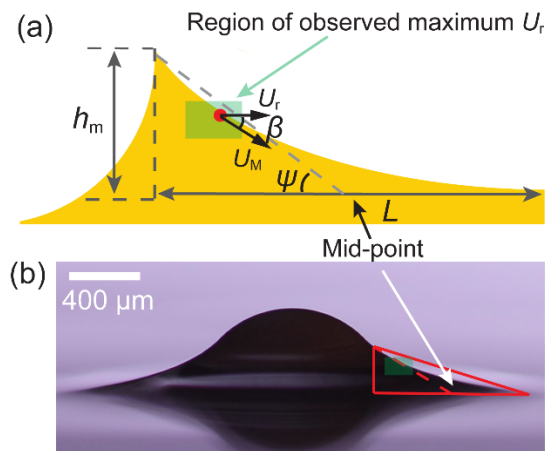

Figure S3. Conversion of U_r into U_M based on oil meniscus geometry. (a) Schematic of location of maximum U_r within oil meniscus. (b) An experimental image from side-view shows the profiles of a central droplet (Glycol) and a 19-cP silicone oil meniscus.

S4 Simulation of heat transfer and fluid dynamics within an oil meniscus

To interpret the fluid flow and temperature field within the oil meniscus, we simulated the conjugate heat transfer and fluid dynamics using COMSOL Multiphysics. As shown in **Fig. S4(a)**, we used a 2D axisymmetric geometry that includes the glass sphere and its oil meniscus. The meniscus profile was imported from the experimental measurements using confocal microscopy. In the simulation, we assigned a no slip boundary condition to the sphere-oil and substrate-oil interfaces and defined the oil-air boundary as a free interface. The Marangoni effect is included by assigning a boundary condition at the oil-air interface[3]:

$$\vec{\mathbf{n}} \cdot [-pI + \mu_o(\nabla \boldsymbol{u} + (\nabla \boldsymbol{u})^T)] \cdot \vec{\mathbf{t}} = -\vec{\mathbf{t}} \cdot \gamma_T \nabla T, \tag{S1}$$

where $\vec{\mathbf{n}}$ is the unit outward normal to the surface, p is the pressure, μ_o is the oil viscosity, $\boldsymbol{u}$ is the velocity vector, $\vec{\mathbf{t}}$ is the orthonormal tangent vector to the interface, T is the temperature, and γ_T is the temperature-dependent surface tension ($\approx$ -5.8×10^{-5} N/(m·K)) of the silicone oil[4]. The term $[-pI + \mu_o(\nabla \boldsymbol{u} + (\nabla \boldsymbol{u})^T)]$ represents the stress tensor.
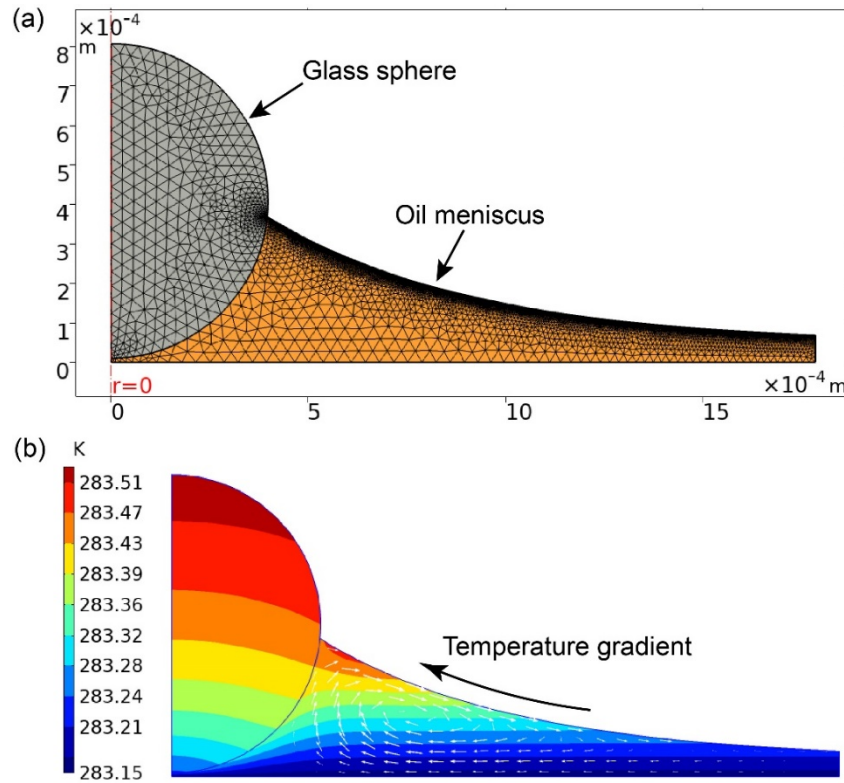

Figure S4. Simulation domain and results. (a) Mesh of the system under consideration, including two domains: solid sphere and liquid oil meniscus. (b) Temperature distribution within the sphere and oil meniscus in cross sectional view. The white arrows are velocity vectors.

The temperature boundary condition for the substrate-oil interface was set as constant temperature (283.15 K) in accordance with the experiments. At the sphere-air and oil-air interfaces, a forced convection thermal boundary condition with the room at 296.15 K (23 °C) was imposed, for which the indoor air flow velocity was assumed to be 0.1 m/s. The silicone oil has a very low vapor pressure (<5 mm Hg at 25 °C), so its evaporation was neglected. The convective flow within the meniscus and the oil-air interfacial temperature distribution were obtained by solving the energy conservation equation in the solid sphere and the mass, momentum, and energy conservation equations in the oil meniscus:

$$\nabla \cdot (\rho \boldsymbol{u}) = 0, \tag{S2}$$

$$\nabla p = \mu_\mathrm{o} \nabla^2 \boldsymbol{u}, \tag{S3}$$

$$\rho c_\mathrm{p} \boldsymbol{u} \cdot \nabla T - \nabla \cdot (k \nabla T) = 0, \tag{S4}$$

where ρ is the density, ∇p is the pressure gradient, c_p is the specific heat capacity at constant pressure, and k is the thermal conductivity. **Figure S4(b)** shows that a vertical temperature gradient establishes along the oil-air interface, inducing a Marangoni convection roll.

S5 Influence of thermal conductivity of the central sphere on oil convection

We experimentally demonstrated that the flow field within the oil menisci depends on the oil meniscus geometry and the substrate temperature. To examine the role of the thermal conductivity of the central sphere, we varied the thermal conductivity of the central sphere and used representative values of common materials: 0.3 W/(m·K) (Teflon), 0.6 W/(m·K) (water), 1.14 W/(m·K) (borosilicate glass) and 15 W/(m·K) (stainless steel), while all other parameters stayed the same. **Figure S5** shows that the interfacial velocity decreases with an increase in thermal conductivity. When $k > 0.6$, the interfacial flow direction is first inward and then becomes outward, featuring a stagnation point in the region of the highest temperature.
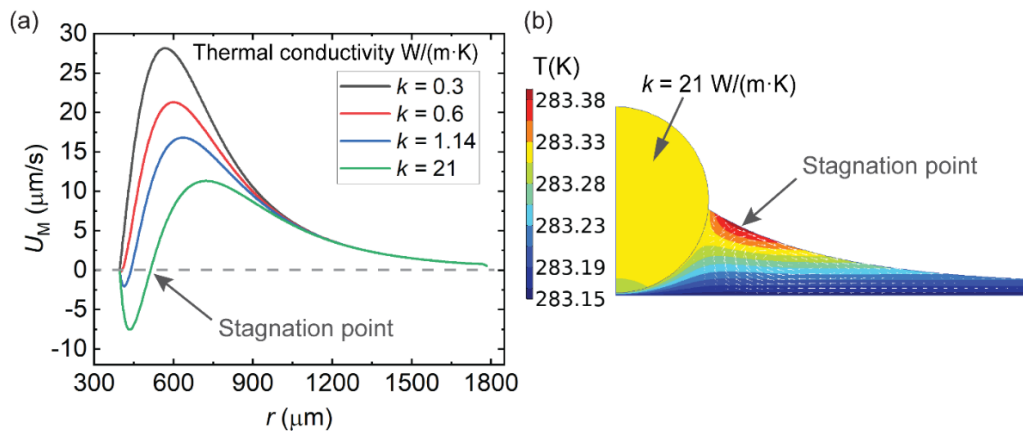

Figure S5. Simulation of Marangoni convection inside oil menisci surrounding central objects with different thermal conductivities. (a) Interfacial velocity along the oil-air interface for thermal conductivities of k = 0.3, 0.6, 1.14 and 21 W/(m·K), respectively. Outward interfacial oil flow is defined as positive. The substrate temperature is set as 283.15 K. Temperature distribution and flow field inside the oil meniscus surrounding a central object with k = 21 W/(m·K).

S6 Negative convection roll in an oil meniscus on a heated substrate
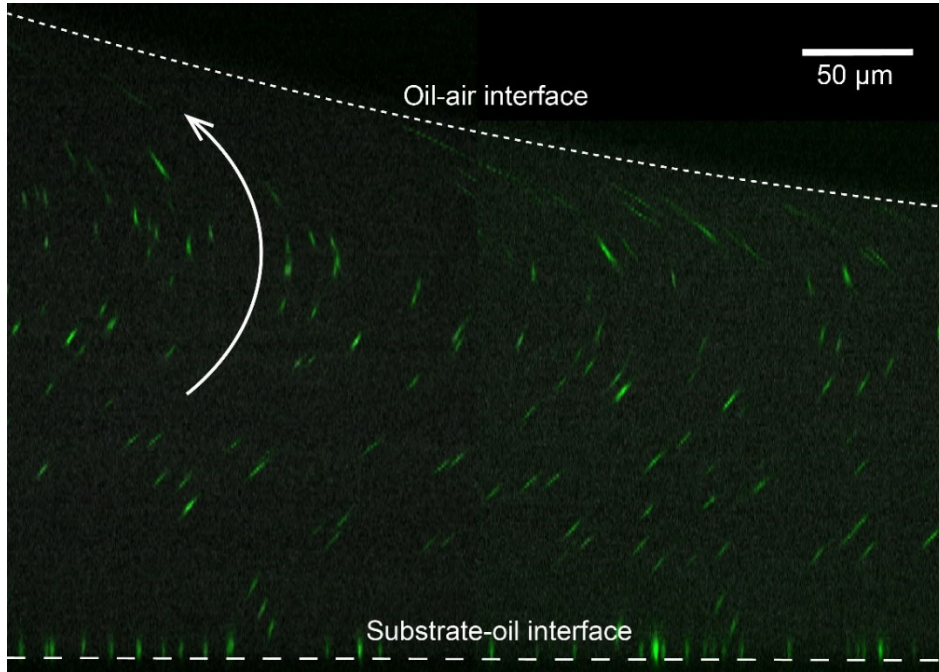

Figure S6. Superimposed orthogonal images from a confocal microscopy z-stack scan of the convection flow in a 48-cP silicone oil meniscus surrounding a 780-μm glass sphere (to the left of this image) on a sapphire substrate held at 35 °C. The oil was dyed with Lumogen Rot F305 and labeled with a low concentration of 1-μm Fluoresbrite YG microspheres. The particle motion can be seen as streamlines, since both the particles and the scanning direction moved from the bottom to the top of the meniscus. One z-scan took approximately 62 milliseconds to complete.

S7 Estimation of (cos φ_F − cos φ_B) for large supported and small floating droplets

The secondary meniscus (belonging to the moving droplet) is modified due to the presence of the curved primary oil meniscus, causing an angle difference (cos φ_F − cos φ_B) and thereby the unbalanced capillary force, as shown in **Fig. S7(a)**. The angle difference for large supported droplets is experimentally measured from side-view during the droplet movement, as shown in **Fig. S7(b),** and is (cos φ_F − cos φ_B) ~10^{-1}. For small floating droplets, (cos φ_F − cos φ_B) is related to the angle difference of the primary meniscus slope between points F and B (intersection of the droplet with the primary meniscus at the front and back, with β_F and β_B, respectively), as illustrated in **Fig. S7(c)**. The angle difference (cos β_F − cos β_B) is determined by the curvature of the primary meniscus and the droplet size. If the oil meniscus were replaced with a flat oil film, (cos φ_F − cos φ_B) = (cos β_F − cos β_B) = 0 for all droplets. Similarly, to small floating droplets, the primary meniscus appears nearly planar. We experimentally measured a meniscus profile and fit it with an exponential expression: $h(r) = 1487 \times e^{-0.004 \times r} + 4.62$ (see **Fig. S7(d)**). Suppose there is a small floating droplet (d = 25 μm) at r = 800 μm from the center of the sphere, we obtain cos φ_F − cos φ_B ≈ cos β_F − cos β_B ≈ 0.004.
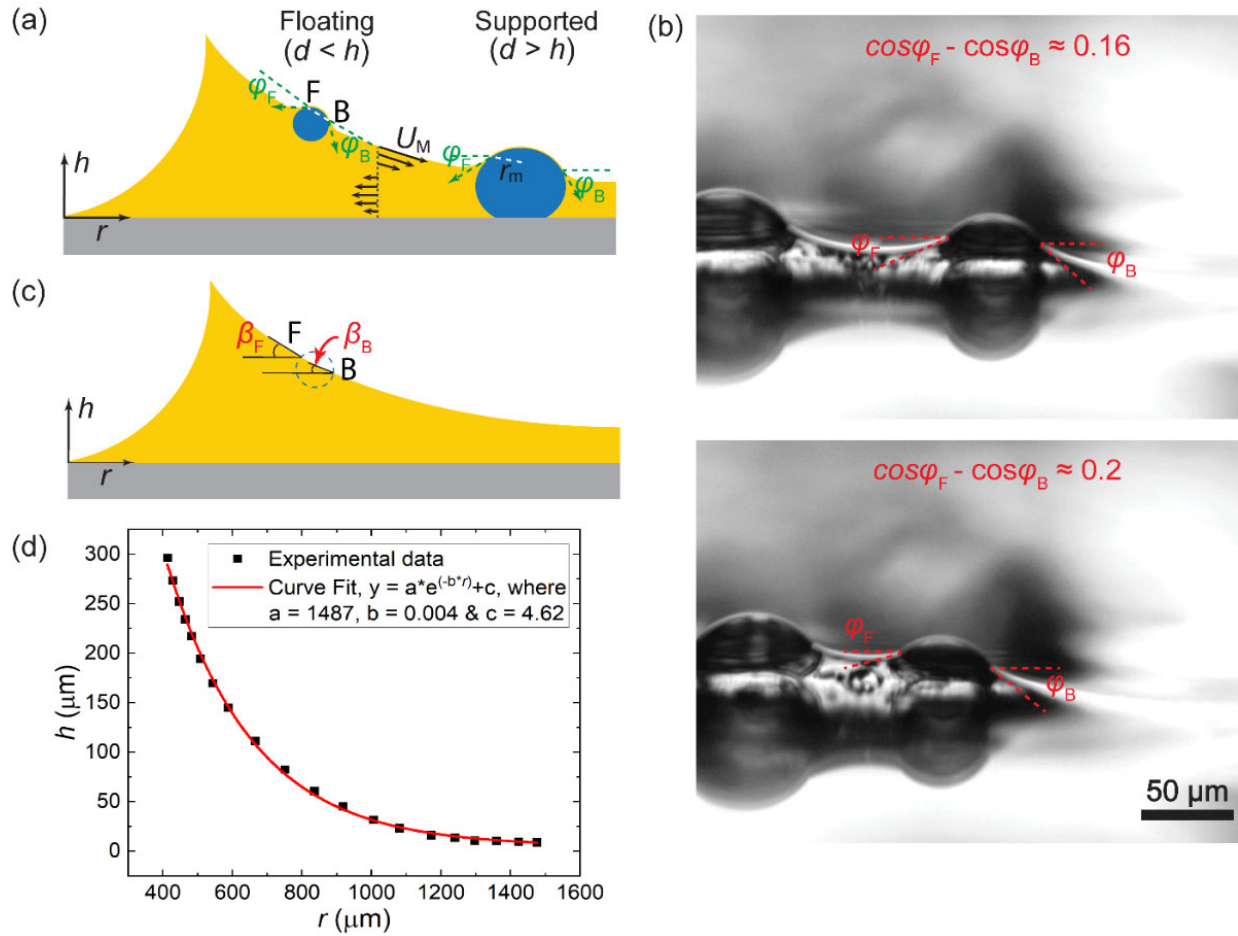
Figure S7. Schematics of the angle difference (cos φ_F – cos φ_B) for large supported and small floating droplets on an oil meniscus. (b) Estimation of the angle difference for a supported droplet during the movement based on side-view images. (c) Approximation of the angle difference for a floating droplet as the local meniscus slopes at points F and B. (d) Exponential fitting of the oil-air interfacial profile of an oil meniscus as experimentally measured by confocal fluorescence microscopy.

S8 Dynamics of droplets initially dispensed closer to the meniscus top
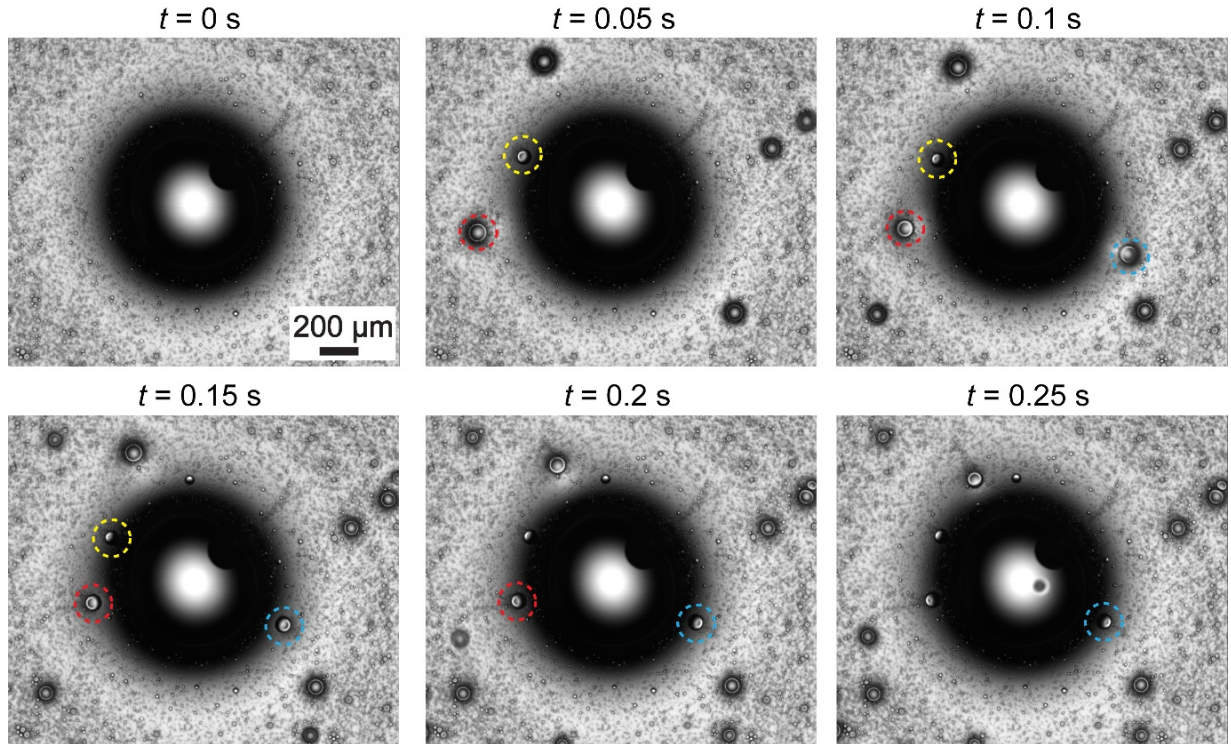

Figure S8. Droplet movements when initially deposited closer the top of the meniscus. An ethylene-glycol droplet with a diameter of 650 um was pre-placed on a LIS with a layer of 19 cP silicone oil (initial thickness ~ 16 μm). Then, water droplets were added to the sample using a mist sprayer and humidifier. Select droplets, which are initially close to the apex of meniscus are highlighted in colorful dashed circles. These large supported droplets still ascend the meniscus and move towards the central droplet.

S9 Determination of fitting factor f

We repeated the simulation outlined in **Section S4** and varied the substrate temperature from 10 to 50°C, with all other parameters staying the same. **Figure S8** shows the temperature variation along the oil-air interface, $\Delta T_{\text{interface}}$, *versus* the temperature difference between substrate and environment, $T_s - T_{\text{env}}$ (*i.e.*, the vertical temperature difference). We define the fitting factor as $f = \Delta T_{\text{interface}} / (T_s - T_{\text{env}})$, which is related to the Biot number $Bi = h_c\sqrt{h_m^2 + L^2}/k_{\text{oil}}$ of the oil film, where h_c is the convective heat transfer coefficient at the oil-air interface and k_{oil} is the thermal conductivity of the oil film.
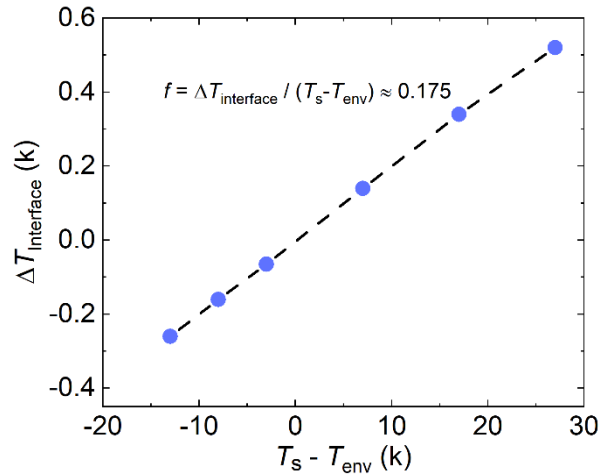
Figure S9. Simulation results of the oil-air interfacial temperature difference along the meniscus arc length as a function of the substrate temperature relative to the environment.

References

1 Z. Dai and D. Vella, *Phys. Rev. Fluids*, 2022, **7**, 054003.
2 H. Teisala, C. Schönecker, A. Kaltbeitzel, W. Steffen, H.-J. Butt and D. Vollmer, *Phys. Rev. Fluids*, 2018, **3**, 084002.
3 S. H. Davis, *Annual Review of Fluid Mechanics*, 1987, **19**, 403–435.
4 S. M. O'Shaughnessy and A. J. Robinson, *International Journal of Thermal Sciences*, 2014, **78**, 101–110.
5 J. Sun and P. B. Weisensee, *Soft Matter*, 2019, **15**, 4808–4817.
6 J. Jiang, J. Gao, H. Zhang, W. He, J. Zhang, D. Daniel and X. Yao, *Proceedings of the National Academy of Sciences*, 2019, **116**, 2482–2487.